PHYSICAL REVIEW B **94**, 201115(R) (2016)

# Concurrent magnetic and structural reconstructions at the interface of (111)-oriented $La_{0.7}Sr_{0.3}MnO_3/LaFeO_3$

I. Hallsteinsen,[1,2] M. Moreau,[1] A. Grutter,[3] M. Nord,[4] P.-E. Vullum,[4,5] D. A. Gilbert,[3] T. Bolstad,[1] J. K. Grepstad,[1] R. Holmestad,[4] S. M. Selbach,[6] A. T. N'Diaye,[2] B. J. Kirby,[3] E. Arenholz,[2] and T. Tybell[1,*]

[1]*Department of Electronics and Telecommunications, NTNU—Norwegian University of Science and Technology, Trondheim 7491, Norway*

[2]*Advanced Light Source, Lawrence Berkeley National Laboratory, Berkeley, California 94720, USA*

[3]*Center for Neutron Research, National Institute of Standards and Technology, Gaithersburg, Maryland 20899, USA*

[4]*Department of Physics, NTNU—Norwegian University of Science and Technology, Trondheim 7491, Norway*

[5]*SINTEF Materials and Chemistry, Trondheim 7491, Norway*

[6]*Department of Material Science and Engineering, NTNU—Norwegian University of Science and Technology, Trondheim 7491, Norway*

(Received 6 July 2016; published 21 November 2016)

We observe an induced switchable magnetic moment of $1.6 \pm 0.40\,\mu_B$/Fe for the nominally antiferromagnetic $LaFeO_3$ extending two to four interface layers into the non–charge transfer system $La_{0.7}Sr_{0.3}MnO_3/LaFeO_3/SrTiO_3(111)$. Simultaneously a mismatch of oxygen octahedra rotations at the interface implies an atomic reconstruction of reduced symmetry at the interface, reaching two to five layers into $LaFeO_3$. Density functional theory of a structure with atomic reconstruction and different correlation strength shows a ferrimagnetic state with a net Fe moment at the interface. Together these results suggest that engineered oxygen octahedra rotations, affecting the local symmetry, affect electron correlations and can be used to promote magnetic properties.

DOI: 10.1103/PhysRevB.94.201115

Interface engineering of oxides is used to promote novel properties such as metallic conduction between two insulators [1,2], and ferromagnetism (FM) between non-FM materials [3,4]. Tailoring magnetic interfaces in a controlled manner is considered a cornerstone of further development of spintronic devices [5]. Until now much attention has been on modified magnetic states due to charge transfer; for example, in superlattices of $CaRuO_3/CaMnO_3$ and $LaNiO_3/LaMnO_3$, charge transfer results in double exchange between $Mn^{3+}/Mn^{4+}$ and induced FM at the interface [6–8]. In (Y, Ca)$Ba_2Cu_3O_7/La_{0.67}Ca_{0.33}MnO_3$ depletion of charge from the Cu-O layers leads to a reconstruction into a FM orbital-ordered system [4]. However, induced FM at Fe has also been observed in nominally nonferromagnetic materials adjacent to $La_{0.7}Sr_{0.3}MnO_3$ (LSMO) [9,10], even though the $d^5$ electronic state of $Fe^{3+}$ prohibits charge transfer. Atomic reconstructions at interfaces, resulting in novel tilt patterns of the oxygen octahedra, have previously been associated with the emergence of new ferroelectric states [11,12], while the coupling between atomic reconstructions and magnetism is relatively unexplored, despite the importance to spintronic device applications [13,14]. The interface between antiferromagnetic (AF) $LaFeO_3$ (LFO) and the half-metal FM LSMO holds promise from an engineering perspective, as charge transfer to the $d^5$ $Fe^{3+}$ is prohibited, while atomic reconstructions due to a mismatch in tilt patterns is expected. The tilt patterns of their oxygen octahedra are not directly compatible, with LFO (S.G. 62, *Pbnm*) and LSMO (S.G. 167, $R\bar{3}c$) having $a^-a^-c^+$ and $a^-a^-a^-$ rotations (Glazer notation), respectively [15]. This mismatch must be accommodated at the interface, likely through atomic reconstructions. In this Rapid Communication, we address how the mismatch in octahedral rotations is accommodated through structural relaxations at the interface leading to the emergence of FM in LFO, in (111)-oriented LSMO/LFO/$SrTiO_3$ (STO) heterostructures. As all the rotation directions of the oxygen octhadera have both in-plane and out-of-plane components at a (111)-oriented interface it is expected that the change from $a^-a^-c^+$ to $a^-a^-a^-$ rotation would have a larger impact on the structure than for a (001)-oriented interface. Indeed we show large rotational changes at the LSMO/LFO interface, no substantial charge transfer, and an induced switchable moment at the Fe atoms. The length scale of structural as well as magnetic reconstructions extends three to five layers into LFO, and the induced magnetic moment is an order of magnitude larger than previously reported for LSMO/LFO(001) [9].

Epitaxial heterostructures of LSMO/LFO/STO(111) were deposited by pulsed laser deposition (PLD) with LSMO and LFO thicknesses of 16 $d_{111}$ monolayers (3.6 nm) each, 7.2 nm in total. Deposition parameters are described in Refs. [16–18], resulting in fully strained (111)-oriented films with atomically smooth step-and-terrace surfaces (see the Supplemental Material [19]). The atomic structure was analyzed by scanning transmission electron microscopy (STEM) using high-angle annular dark-field (HAADF), annular bright field (ABF), and electron energy loss spectroscopy (EELS). Scanning distortions were reduced by using nonrigid registration [20] and EELS processing was done using HYPERSPY [19,21]. Density functional theory (DFT) calculations were done with the Vienna *ab initio* simulation package (VASP) using the PBE-sol functional and a plane-wave cutoff energy of 550 eV [22–24]. The projected augmented wave - Perdew Burke Ernzerhof (PAW-PBE) potentials supplied with VASP for La, Sr, Mn, Fe, and O with electron configurations $4s^24p^65d^16s^2$, $4s^24p^65s^2$, $3d^54s^2$, $3d^64s^2$, and $2s^22p^4$ respectively were used and different configurations of La and Sr in LSMO were tested [25]. Hubbard $U$ of 10 and 3 eV were applied to the La 4$f$ and Mn 3$d$ orbitals, respectively [26]. Calculations of LFO were done with a 60-atom $\sqrt{2} \times \sqrt{6} \times 2\sqrt{3}$

*Corresponding author: thomas.tybell@ntnu.no

 

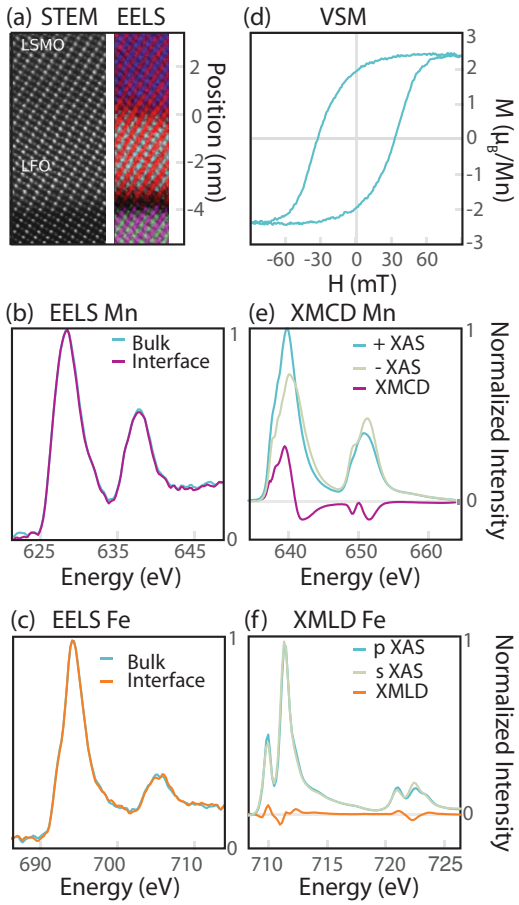


FIG. 1. (a) STEM HAADF image (left) and EELS map (right) colored by element, i.e., La ( red), Mn (purple), Fe (turquoise), Sr (pink), and Ti (green). (b,c) show EELS spectra of $L_{2,3}$ edge of Mn (Fe) at the interface [purple (orange)] and in the center of the layer (turquoise). (d) Hysteresis curve of the bilayer recorded at 50 K. (e,f) XA of different circular (linear) polarization and XMCD (XMLD) spectra of Mn (Fe) $L$ edge.

supercell, while the interface was modeled with 12/12 (LFO/LSMO) 240-atom $\sqrt{2} \times \sqrt{6} \times 8\sqrt{3}$ supercells, with corresponding gamma-centered $k$-point mesh of $4 \times 3 \times 2$ and $4 \times 3 \times 1$, respectively. The in-plane lattice parameters were locked to the calculated equilibrium value of STO, while the out-of-plane lattice parameter and atomic positions were relaxed until the forces on the ions were below 0.01 eV/Å.

To investigate charge transfer across the interface, Bader charges [27] were calculated for LSMO/LFO supercells. For Fe, a small change in Bader charge, 3.03+ from 3+ in bulk, is observed in the unit cell closest to the interface. A small change in Fe valence is expected for Fe-terminated LFO, since this layer effectively corresponds to a mixed LSFO layer, while for the opposite termination the calculations reveal no change in Fe valence. For Mn the Bader charge is increased to 3.375+ (from 3.3+) at the interface, indicating an increased amount of $Mn^{4+}$. Experimental STEM HAADF reveal that the heterostructure is epitaxial, fully strained, and of high crystalline quality and EELS maps reveal a sharp LSMO/LFO interface with no substantial intermixing of cations [Fig. 1(a)], unlike the LFO/STO interface which is intermixed [18,19]. A comparison of EELS spectra at the bulk and at the interface reveals no change in the Mn and Fe valence state, indicating no charge transfer within the measurement sensitivity [Figs. 1(b) and 1(c)].

The magnetic ground state of the thin films was probed using a vibrating sample magnetometer after a 2 T field cooling to 50 K from room temperature; in Fig. 1(d) a hysteresis at 50 K is shown. The saturation magnetization is 2.4 $\mu_B$/Mn, assuming Mn as the only contribution to the magnetic signal and the coercive field is 37.5 mT. The Curie temperature, $T_c$, was 275 K [19]. X-ray magnetic circular dichroism (XMCD) and x-ray magnetic linear dichroism (XMLD) spectroscopy were measured at beamline 4.0.2 and 6.3.1 at the Advanced Light Source (ALS) and I1011 at MaxLab II. The spectra shown were measured in total-electron-yield mode by monitoring the sample drain current, with the x rays incident at 30° to the sample surface. Using an eight-pole electromagnet, XMCD was measured with an applied field of ±0.3 T parallel to the x-ray beam. For XMLD, $s$ and $p$ polarization of the beam was used. Figures 1(e) and 1(f) depict the absorption spectra for the Mn and Fe $L$ edge, respectively, with spectral shapes in agreement with reported spectra for single-layer films with $Mn^{3.3+}$ and $Fe^{3+}$ valence state [28,29]. XMCD/XMLD was adopted to probe the element-specific FM/AF; Mn XMCD spectra confirm FM ordering (30% XMCD) and Fe XMLD spectra indicate AF ordering with 5% XMLD (similar to single-layer LFO). LFO in bulk is a $G$-type AF, with fully spin polarized (111) planes. The coercive field of the bilayer is increased compared to single layers of LSMO [30]; however, no exchange bias was observed. The dichroism of Fe indicates a canted out-of-plane AF axis, in agreement with (111) $(La,Sr)FeO_3$, which also exhibited no exchange bias [31].

Having established the magnetic states for the individual constituents of the heterostructure we turn to structural effects at the interface, focusing on the LFO. Figure 2(a) shows schematics of the oxygen octahedral rotations for STO ($a^0a^0a^0$), LFO ($a^-a^-c^+$), and LSMO ($a^-a^-a^-$). At the LSMO/LFO interface half of the octahedra match (tilt the same way), while the other half do not (tilt the opposite way). STEM HAADF and ABF imaging along the $[1\bar{1}0]$-zone axis were used to probe the atomic positions [Figs. 2(b) and 2(d)]. In Fig. 2(c) the eccentricity (deviation from a circle) of the $A$-cation columns are plotted as a function of position with respect to the LSMO/LFO interface. In LFO a large eccentricity is expected due to the distortion of the unit cell. As expected, the eccentricity peaks in the center of the LFO layer, and is reduced near both interfaces. However, the change is not abrupt, and two to three layers of LFO close to the LSMO interface have a reduced eccentricity compared to the center of the LFO. Another measure of deviation from the cubic structure is the displacement of the oxygen columns along the [100] direction, where LFO should have a displacement of 35 pm. In Fig. 2(e) it is clear that the amplitude of the displacements decreases throughout both interfaces, beginning roughly at the second layer of LFO, hence these layers have a reduced displacement. Combining the oxygen displacement and $A$-cation eccentricity data, the analysis suggests that two to three interface layers of LFO have a reduced distortion compared to bulk. DFT simulations of the octahedral rotation angle along the $c$ axis ($\gamma$) across the LSMO/LFO interface

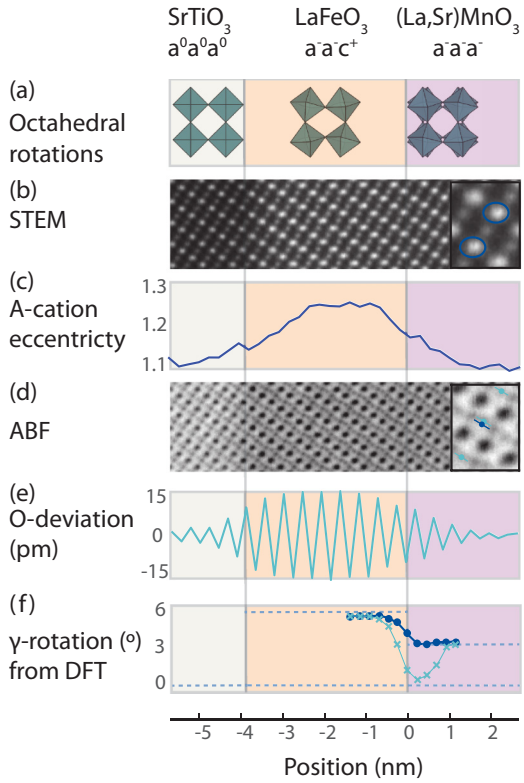


FIG. 2. (a) Schematic of the octahedral rotations in STO ($a^0a^0a^0$), LFO ($a^-a^-c^+$), and LSMO ($a^-a^-a^-$) shown from the [001] direction [33]. (b) STEM-HAADF image. Inset shows the enlarged view of the elliptical form of the La columns in LFO. (c) Plot of the *A*-cation eccentricity (d) STEM-ABF image. Inset shows an enlarged view of oxygen positions in the layer ( turquoise) and the deviation from a cubic structure (blue). (e) Plot of the oxygen column displacement along [100], integrated for monolayers in the [111] direction. (f) Plot of the calculated $\gamma$ rotation for matched (dark blue) and mismatched (turquoise) octahedra. All plots are shown as a depth profile through the bilayer, and are matched to the TEM images as shown by the gray lines and colored boxes.

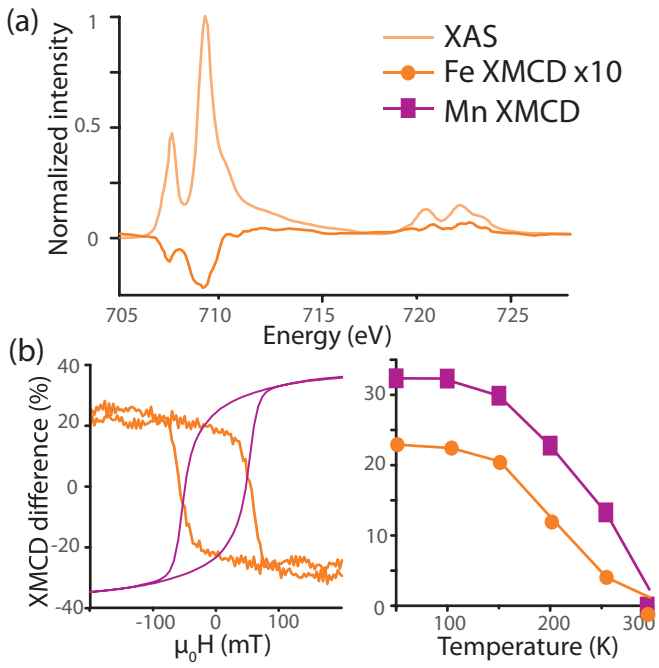


FIG. 3. (a) XA and XMCD spectra at the Fe *L* edge. (b) Field (left) and temperature (right) dependence of Fe *L*3 XMCD (orange) and Mn *L*3 XMCD (purple).

are presented in Fig. 2(f), where the matching octahedra (dark blue) and the nonmatching octahedra (light blue) evolve differently. While the rotations of the matched octahedra relax to the bulk value for both materials, the rotation angle of the mismatched octahedra drops toward zero. The tilt pattern at the interface is hence close to the $a^-a^-c^0$ tilt pattern for half the octahedra. The reduced rotation angle prevails two to four layers into the LFO, in accordance with the experimental data.

To investigate if the observed structural changes at the interface have influence on the magnetic properties, XMCD spectroscopy probing ferromagnetic order was performed at the Fe *L* edge [Fig. 3(a)]. We observe a circular dichroism signal of approximately 2% of the Fe L3 normalized absorption peak (XA) signal at 50 K. Measurements were done with alternating polarization of the x rays under a static field and in remanence, as well as with alternating field with a static polarization resulting in the same magnitude and shape of the dichroism signal. Monitoring the field dependence of the Fe and Mn *L*3 XMCD in hysteresis loops [Fig. 3(c)] reveals that Mn and Fe are antiparallel and with equal coercive fields of approximately 70 mT at 50 K. This is in agreement with Bruno *et al.* [9], who demonstrated an induced FM moment in LFO with an antiparallel coupling to LSMO for LSMO/LFO(001). In Fig. 3(d) we have plotted the temperature dependence of the Mn and Fe *L*3 XMCD. The Fe XMCD signal follows that of Mn, with a comparable $T_c$, although the Néel temperature of LFO is much higher (740 K). The similar coercive field and Curie temperature observed for both Mn and Fe strongly suggest that the FM moment of Fe is stabilized by a coupling with the LSMO layer. Although FM systems also have a XMLD response the Fe-XMLD signal is larger than the XMCD signal for Fe, implying a predominantly AF LFO layer.

In order to investigate the depth profile of the magnetic structure we used polarized neutron reflectivity (PNR) performed using the PBR beamline at NIST Center for Neutron Research. Measurements were conducted at 50 K after field cooling in 700 mT, using an in-plane measurement field of 700 mT. The spin of the incident neutrons was polarized parallel or antiparallel to the in-plane magnetic field *H*, and the specular reflectivity was measured as a function of wave-vector transfer along the surface normal $Q_z$. The model-fitted non-spin-flip reflectivities are depicted in Fig. 4(a). In this scattering geometry the non-spin-flip reflectivity is a function of the nuclear and magnetic scattering length density (SLD) depth profiles, where the magnetic SLD is directly proportional to the magnetization component parallel to *H*, and not sensitive to AF ordering. We find a splitting of the two channels, indicating sensitivity to the sample magnetization. The PNR data were modeled using the REFL1D software package [32], and the resulting depth profile is shown in Fig. 4(b). It is clear that LSMO is FM with a positive magnetic SLD throughout the film, while at the LFO interface the magnetic SLD is negative for several layers, before relaxing to 0. Hence,

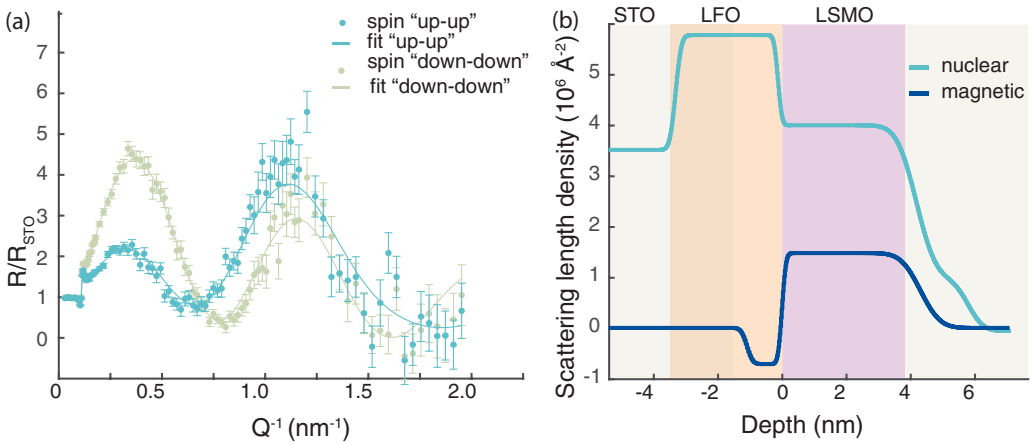


FIG. 4. (a) Neutron reflectivity (crosses) and fits (line) measured in the non-spin-flip geometry, with neutrons polarized with spin up (blue) and spin down (green) with respect to the external field. (b) Magnetic and nuclear depth profile derived from the neutron scattering data.

the LFO has clearly a remanent moment at the interface antiparallel to the LSMO, in agreement with the XMCD measurements. For comparison, we also fit the PNR to a model with zero net magnetization in the LFO layer, which resulted in a significantly poorer fit (see [19]). The fitted PNR model with a 95% confidence interval shows that the induced moment reaches between 0.64 and 1.19 nm (three to five $d_{111}$ monolayers) into LFO. The FM moment of LSMO was found to be $3.1 \pm 0.06\,\mu_B$/Mn, while the LFO moment was found to be $1.6 \pm 0.40\,\mu_B$/Fe. However, the value is smaller than the nominal AF moment of $4.5\,\mu_B$/Fe, suggesting a canted AF or ferrimagnetic state at the interface.

The length scales of the induced FM moment and the structural reconstruction are both around two to five layers into LFO. *G*-type AF order is found to be 313 meV/f.u. lower in energy than FM order from DFT calculations on pure LFO. Although this confirms that *G*-type AF is very stable in bulk LFO, a different local symmetry is enforced at the (111)-LFO/LSMO interface, possibly affecting the electron correlations. By taking the Hubbard $U$ enforced on Fe as a measure of the correlation strength, we compare the energy difference between the FM and AF states for different rotation patterns [Fig. 5(a)]. Interestingly, we find that as $U_{Fe}$ approaches zero a FM state is stabilized. This ferromagnetic state is stable for the $a^-a^-a^0$ rotations resembling the tilt pattern observed at the interface [Fig 2(e)], but not for the bulk $a^-a^-c^+$ rotations. For a 12/12 LFO/LSMO superlattice, including the effects of the interface and symmetry mismatch, the lowest energy is still found for the bulk *G*-type AF. FM-ordered Fe layers at the interface are metastable with an energy cost of ∼45 meV/Fe for each FM layer, and the lowest value for parallel Mn and Fe moments. With a nominal $U_{Mn}$ of 3 eV, Bader charge analysis revealed that the Mn closest to the LFO has a larger fraction of $Mn^{4+}$ compared to the rest of the cell, inconsistent with the EELS measurements. To impose a 3.3+ Mn valence increased values of Hubbard $U$ at the interface ($U_{Mn,I}$) are investigated, which result in an AF ground state with a FM moment at the interface. As seen in Fig. 5(b), the net FM moment for Fe increases with increasing $U_{Mn,I}$. For pure LFO a net FM moment was found for decreased $U_{Fe}$; in Fig. 5(b) we plot the effect of lowering $U_{Fe}$ for the two Fe layers closest to the interface ($U_{Fe,I}$), keeping $U_{Mn}$ constant at 3 eV. The result is a switchable moment which is increased as $U_{Fe,I}$ is lowered. In the right panel of Fig. 5(b) these two effects are combined; with the Fe moments as a function of $U_{Fe,I}$ with $U_{Mn,I} = 5$ eV. As we reduce the $U_{Fe,I}$ and increase $U_{Mn,I}$ we reduce the degree of electron localization of the Fe $3d$ electrons and obtain a net FM Fe moment. Though the AF structure is not affected by the direction of the Mn, the FM Fe moment is switchable and antiparallel to the Mn moment,

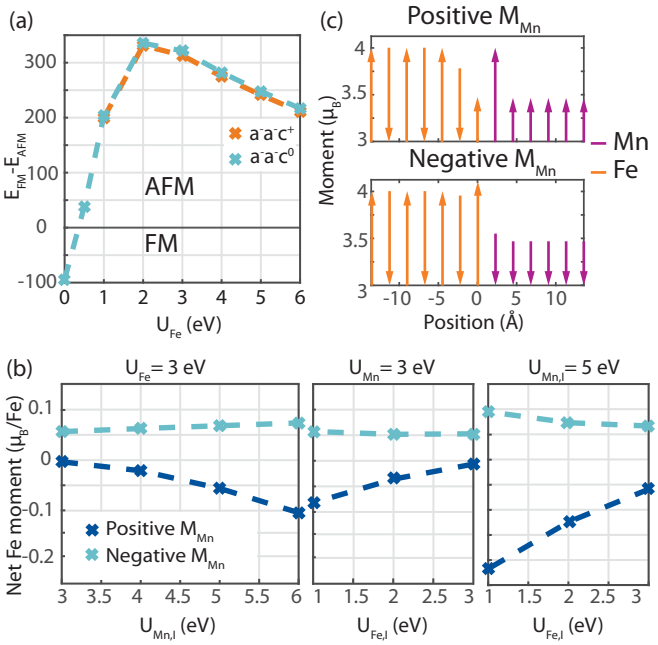


FIG. 5. (a) Energy difference between FM and AF order of LFO as a function of Hubbard $U$ for different rotation patterns. A positive value means that AF ordering is preferred. Note that the $a^-a^-c^+$ rotation is not stable for $U < 1$ eV. (b) Net Fe moment as a function of $U_{Mn,I}$ and $U_{Fe,I}$ in the LSMO/LFO supercell. The first panel shows the dependence on $U_{Mn,I}$ with $U_{Fe}$ constant 3 eV, the second panel $U_{Fe,I}$ with $U_{Mn} = 3$ eV, and the third pane $U_{Fe,I}$ with $U_{Mn,I} = 5$ eV. (c) Atomic magnetic moments as a function of distance from the LSMO/LFO(111) interface with $U_{Mn,I} = 5$ eV and $U_{Fe,I} = 1$ eV.

in agreement with experimental results. The DFT calculations reveal a ferrimagnetic ordering of LFO adjacent to the interface [Fig. 5(c)], where the Fe moment decreases with each layer as we draw nearer to the interface. With $U_{\mathrm{Mn,I}} = 5\,\mathrm{eV}$ and $U_{\mathrm{Fe,I}} = 1\,\mathrm{eV}$ we find a FM moment from $-0.22\,\mu_{\mathrm{B}}$/Fe to $0.09\,\mu_{\mathrm{B}}$/Fe. As we switch the direction of the Mn moment the effect on the Fe moment is not symmetric; the induced moment is lower when the Mn moment is parallel to the second layer of Fe as compared to the first Fe layer. This can be understood for the reason that the degree of localization is mainly reduced on the Fe layer that matches the Mn moment, and this effect is reduced with the separation from the LSMO interface [19]. The DFT calculations are consistent with a change of the LFO and LSMO symmetry resulting in a ferrimagnetic LFO ground state AF coupled to LSMO, with the magnitude of the moment sensitive to the correlation strength.

In summary, the noncompatible oxygen octahedral rotations of (111)-oriented LFO and LSMO result in atomic reconstructions at the interface, inducing $a^-a^-c^0$ octahedral rotation symmetry in the last two to four LFO layers near the interface. These reconstructions affect the electron correlations, as inferred from DFT modeling leading to a ferrimagnetic LFO ground state with AF coupling between the FM Fe and Mn. This finding is supported by XMCD, XMLD, and PNR data. This work shows the importance of structural distortions at epitaxial interfaces in forming magnetic states, and highlights the need to better understand the effect of interfaces on correlation strengths.

T.T. and T.B. acknowledge Research Council of Norway Grant No. 231290. M.N. is supported by the Project NORTEM (Grant No. 197405) within the Programme INFRA- STRUCTURE of the Research Council of Norway. The Norwegian Metacenter for Computational Science (UNINETT Sigma2) was acknowledged for providing computational resources for DFT calculations through Project No. NN9301K. The Advanced Light Source is supported by the Director, Office of Science, Office of Basic Energy Sciences, of the U.S. Department of Energy under Contract No. DE-AC02-05CH11231. Part of this work was performed at the I1011 beamline at MAX II, Sweden, and we thank Gunnar Öhrwall for his assistance at the beamline.

[1] A. Ohtomo and H. Y. Hwang, Nature **427**, 423 (2004).
[2] H. Y. Hwang, Y. Iwasa, M. Kawasaki, B. Keimer, N. Nagaosa, and Y. Tokura, Nat. Mater. **11**, 103 (2012).
[3] A. Brinkman, M. Huijben, M. van Zalk, J. Huijben, U. Zeitler, J. C. Maan, W. G. van der Wiel, G. Rijnders, D. H. A. Blank, and H. Hilgenkamp, Nat. Mater. **6**, 493 (2007).
[4] J. Chakhalian, J. W. Freeland, G. Srajer, J. Strempfer, G. Khaliullin, J. C. Cezar, T. Charlton, R. Dalgliesh, C. Bernhard, G. Cristiani, H.-U. Habermeier, and B. Keimer, Nat. Phys. **2**, 244 (2006).
[5] M. Gibert, P. Zubko, R. Scherwitzl, J. Íñiguez, and J.-M. Triscone, Nat. Mater. **11**, 195 (2012).
[6] K. S. Takahashi, M. Kawasaki, and Y. Tokura, Appl. Phys. Lett. **79**, 1324 (2001).
[7] A. J. Grutter, H. Yang, B. J. Kirby, M. R. Fitzsimmons, J. A. Aguiar, N. D. Browning, C. A. Jenkins, E. Arenholz, V. V. Mehta, U. S. Alaan, and Y. Suzuki, Phys. Rev. Lett. **111**, 087202 (2013).
[8] M. Gibert, M. Viret, A. Torres-Pardo, C. Piamonteze, P. Zubko, N. Jaouen, J.-M. Tonnerre, A. Mougin, J. Fowlie, S. Catalano, A. Gloter, O. Stéphan, and J.-M. Triscone, Nano Lett. **15**, 7355 (2015).
[9] F. Y. Bruno, M. N. Grisolia, C. Visani, S. Valencia, M. Varela, R. Abrudan, J. Tornos, A. Rivera-Calzada, A. A. Ünal, S. J. Pennycook, Z. Sefrioui, C. Leon, J. E. Villegas, J. Santamaria, A. Barthélémy, and M. Bibes, Nat. Commun. **6**, 6306 (2015).
[10] P. Yu, J. S. Lee, S. Okamoto, M. D. Rossell, M. Huijben, C. H. Yang, Q. He, J. X. Zhang, S. Y. Yang, M. J. Lee, Q. M. Ramasse, R. Erni, Y. H. Chu, D. A. Arena, C. C. Kao, L. W. Martin, and R. Ramesh, Phys. Rev. Lett. **105**, 027201 (2010).
[11] H. Wang, J. Wen, D. J. Miller, Q. Zhou, M. Chen, H. N. Lee, K. M. Rabe, and X. Wu, Phys. Rev. X **6**, 011027 (2016).
[12] E. J. Moon, R. Colby, Q. Wang, E. Karapetrova, C. M. Schlepütz, M. R. Fitzsimmons, and S. J. May, Nat. Commun. **5**, 5710 (2014).
[13] Z. Liao, M. Huijben, Z. Zhong, N. Gauquelin, S. Macke, R. J. Green, S. Van Aert, J. Verbeeck, G. Van Tendeloo, K. Held, G. A. Sawatzky, G. Koster, and G. Rijnders, Nat. Mater. **15**, 425 (2016).
[14] A. J. Grutter, A. Vailionis, J. A. Borchers, B. J. Kirby, C. L. Flint, C. He, E. Arenholz, and Y. Suzuki, Nano Lett. **16**, 5647 (2016).
[15] A. M. Glazer, Acta Crystallogr., Sect. B **28**, 3384 (1972).
[16] I. Hallsteinsen, J. E. Boschker, M. Nord, S. Lee, M. Rzchowski, P. E. Vullum, J. K. Grepstad, R. Holmestad, C. B. Eom, and T. Tybell, J. Appl. Phys. **113**, 183512 (2013).
[17] J. E. Boschker, E. Folven, A. F. Monsen, E. Wahlström, J. K. Grepstad, and T. Tybell, Cryst. Growth Des. **12**, 562 (2012).
[18] I. Hallsteinsen, M. Nord, T. Bolstad, P.-E. Vullum, J. E. Boschker, P. Longo, R. Takahashi, R. Holmestad, M. Lippmaa, and T. Tybell, Cryst. Growth Des. **16**, 2357 (2016).
[19] See Supplemental Material at http://link.aps.org/supplemental/10.1103/PhysRevB.94.201115 for more information about deposition, transmission electron microscopy measurements, spin-polarized neutron reflection measurements, and density functional theory calculations.
[20] L. Jones, H. Yang, T. J. Pennycook, M. S. J. Marshall, S. Van Aert, N. D. Browning, M. R. Castell, and P. D. Nellist, Adv. Struct. Chem. Imaging **1**, 1 (2015).
[21] F. de la Peña, P. Burdet, T. Ostasevicius, M. Sarahan, M. Nord, V. T. Fauske, J. Taillon, A Eljarrat, S Mazzucco, G. Donval, L. F. Zagonel, M. Walls, and I. Iyengar, HYPERSPY 0.8.2 (2015).
[22] G. Kresse and D. Joubert, Phys. Rev. B **59**, 1758 (1999).
[23] G. Kresse and J. Furthmüller, Phys. Rev. B **54**, 11169 (1996).
[24] J. P. Perdew, A. Ruzsinszky, G. I. Csonka, O. A. Vydrov, G. E. Scuseria, L. A. Constantin, X. Zhou, and K. Burke, Phys. Rev. Lett. **100**, 136406 (2008).
[25] D. S. Mark, M. C. Adam, M. R. James, and J. M. Steven, J. Phys.: Condens. Matter **26**, 505502 (2014).
[26] S. L. Dudarev, G. A. Botton, S. Y. Savrasov, C. J. Humphreys, and A. P. Sutton, Phys. Rev. B **57**, 1505 (1998).

[27] G. Henkelman, A. Arnaldsson, and H. Jónsson, Comput. Mater. Sci. **36**, 354 (2006).

[28] J. Lüning, F. Nolting, A. Scholl, H. Ohldag, J. W. Seo, J. Fompeyrine, J. P. Locquet, and J. Stöhr, Phys. Rev. B **67**, 214433 (2003).

[29] Y. Takamura, R. V. Chopdekar, E. Arenholz, and Y. Suzuki, Appl. Phys. Lett. **92**, 162504 (2008).

[30] I. Hallsteinsen, E. Folven, F. K. Olsen, R. V. Chopdekar, M. S. Rzchowski, C. B. Eom, J. K. Grepstad, and T. Tybell, APL Mater. **3**, 062501 (2015).

[31] Y. Jia, R. V. Chopdekar, E. Arenholz, A. T. Young, M. A. Marcus, A. Mehta, and Y. Takamura, Phys. Rev. B **92**, 094407 (2015).

[32] http://www.ncnr.nist.gov/reflpak

[33] K. Momma and F. Izumi, J. Appl. Crystallogr. **44**, 1272 (2011).